

Research Article

Reproduction of Local Strong Wind Area Induced in the Downstream of Small-Scale Terrain by Computational Fluid Dynamic (CFD) Approach

Takanori Uchida ¹ and Keiji Araki²

¹Research Institute for Applied Mechanics (RIAM), Kyushu University, 6-1 Kasuga-kouen, Kasuga, Fukuoka 816-8580, Japan

²Meteorological Disaster Prevention Group Railway Technical Research Institute (RTRI), 2-8-38 Hikari-cho, Kokubunji, Tokyo 185-8540, Japan

Correspondence should be addressed to Takanori Uchida; takanori@riam.kyushu-u.ac.jp

Received 22 April 2019; Revised 2 August 2019; Accepted 17 September 2019; Published 4 December 2019

Academic Editor: Parviz Ghadimi

Copyright © 2019 Takanori Uchida and Keiji Araki. This is an open access article distributed under the Creative Commons Attribution License, which permits unrestricted use, distribution, and reproduction in any medium, provided the original work is properly cited.

In this research, the computational fluid dynamic (CFD) approach was applied for the solution of the problems of local strong wind areas in railway fields, and the mechanism of wind generation was discussed. The problem of local wind occurring on a railway line in winter was taken up in this research. A computational simulation for the prediction of wind conditions by large-eddy simulation (LES) was implemented, and it was clarified that local strong wind areas are mainly caused by separated flows originating from small-scale terrain positioned at its upstream (at approximately 180 m above sea level). Meanwhile, the effects of the size of the calculation area and spatial grid resolution on the result of calculation and the effect of atmospheric stability were also discussed. It was clarified that in order to simulate the air flow characteristic of the separated flow originating from the small-scale terrain (at an altitude of approximately 180 m) targeted in the present research, approximately 10 m of spatial resolution of computational cell in the horizontal direction is required. In addition, the effect of stable stratification on the flow was also examined. As a result, lee waves were excited at the downstream of the terrain over time in the case of stably stratified flow ($Fr = 1.0$). The reverse-flow region lying behind the terrain, which had been observed at a neutral time, was strongly inhibited. Consequently, a local strong wind area was generated at the downstream of the terrain, and a strong wind area passing through the observation mast was observed. By investigating the increasing rate of speed of the local strong wind area induced at the time of stable stratification, it was found that the wind was approximately 1.2 times stronger than what was generated at a neutral time.

1. Introduction

At present, the wind power generation business is rapidly growing at an unprecedented rate around the world. This is due to it having the best cost performance in attaining the avoidance of fossil fuels and the reduction of CO₂ generation among all renewable energies. In Japan, wind power generation is also the leading source of renewable energy; the further prevalence of wind power generation throughout the world will surely contribute to the overcoming of global warming (green innovation). One of the technical problems to be solved in the future in the field of wind power generation is to correctly understand the local wind conditions

which are generated around wind turbines and establish a computational wind prospecting technology with higher accuracy than before that can be applied to the survey before the introduction of wind turbines [1–11]. The author's group narrowed the scales down from several m to several km and is developing a computational wind prospecting model that can reproduce local wind conditions with high accuracy (RIAM-COMPACT) [12–21]. By employing LES (large-eddy simulation) for the turbulence model, it becomes possible to reproduce nonsteady wind conditions that change temporally and spatially.

Recently, the number of accidents regarding wind turbines in onshore wind farms constructed on complex terrain

has been rapidly increasing. According to a recent survey conducted by the author and others, it has been pointed out that these wind turbine accidents are strongly related to topographic turbulence (a turbulent flow field originating from the terrain). In addition to the problem of topographic turbulence, as mentioned above, multiple large-scale wind turbines which are intensively constructed in mountainous regions for onshore wind farms are actual situations in Japan which cannot be avoided. Therefore, in order to prevent the lowering of the entire amount of electric power generated in a wind farm caused by the mutual intervention of each wind turbine, the development of a wake model that determines the appropriate distance between wind turbines has become the most important subject for future investigation. In the case of offshore wind farms, which have been attracting attention, the problem of the distance between wind turbines, i.e., the most appropriate arrangement of wind turbines, has become apparent.

In this research, the computational fluid dynamic approach, which has been applied to the field of wind power generation, was applied to the problem of local strong wind areas in railway fields, and its generation mechanism was discussed. In tandem, the effectiveness of the application of the computational fluid dynamics approach to railway fields was discussed. The railway industry has also had problems with the strong wind that occurs along railway tracks [22–28]. More than 50 cases of accidental derailing and rollover caused by strong wind have been recorded in Japan, including one that occurred on the present Tokaido Line in 1889 (Meiji 22). The measures against strong wind in railway fields mainly consist of structural measures (improvement of windbreak fences) and nonstructural measures (operating rules). These measures have been developed through the lessons learnt from these accidents. At present, strong wind monitoring along railways is conducted by observing the instantaneous wind speed with an anemometer. This is because the investigation of accidental derailing and rollover on the Sanin Main Line that occurred in 1986 verified that what greatly affects the accidents is the instantaneous wind speed.

The railways in Japan thread through narrow and steep terrain, and their environments also change from country areas to city areas to mountain areas. In the downwind region of complex terrain, in particular, once strong winds occur, there is a fear of intensifications of wind caused by topographic effects and topographic turbulence. In order to prevent trains from derailing and rolling over, it is important to linearly evaluate the strong wind that occurs in the environment along railway tracks by its instantaneous wind speed; however, for that purpose, it is not enough only to measure the wind along railways using an anemometer, the analysis of nonsteady wind condition by CFD is also required.

In this research, the problem of the local strong wind which occurs on the railway line in winter was taken up. On the railway line, the problems of the delays of trains at times of strong wind in winter are often discussed. Against these problems, the characteristics of the wind conditions of local strong wind areas generated around railway lines were

discussed based on the measured data and the weather grid point value (GPV) data. The direction of the wind generated in strong wind areas, in particular, was estimated. After that, wind conditions in the narrow space of a several dozen km or less were reproduced using computational wind prospecting technology (RIAM-COMPACT), and the mechanism of local strong wind generation was discussed. At the same time, the effects of the size of the calculation area and spatial grid resolution on the result of calculation were also discussed. Finally, the effect of atmospheric stability was discussed.

The structure of this paper is as follows. Section 2 explains the wind condition characteristics by measured data and weather GPV data. Section 3 explains the outline of numerical calculation technique. Section 4 explains the calculation results and discussion. Section 5 explains the effects of size of calculation area and grid resolution in the horizontal direction. Section 6 explains the effect of atmospheric stability. Finally, Section 7 is the conclusion.

2. Wind Condition Characteristics of Local Wind Conditions by Measured Data and Weather GPV Data

Figure 1 shows the locations of the railway line and observation mast and the evaluation points of the weather GPV data in the neighborhood of observation mast. For measuring data, only a wind speed sensor was installed at the top of the observation mast, 5 m above ground, but no wind direction sensor was installed. The period of data recording was nine months from July 2014 to March 2015. For the verification of these measured data, LFM_S (local forecast mode; S refers to surface data), which comprises weather GPV (grid point value data) at 10 m above ground with a spatial resolution of 2 km, provided by Japan Meteorological Agency, was used. In this research, the weather GPV data at the point (longitude 130.15 degrees and latitude 33.52 degrees) nearest to the observation mast (longitude 130.1503333 degrees and latitude 33.5245 degrees) were used. The horizontal distance between the points of the observation mast and weather GPV data was approximately 500 m.

Figure 2 shows the time variations (one-hour time interval) of wind speed and wind direction during the entire period of data collection (nine months from July 2014 to March 2015). Regarding wind speed, the measured data (5 m above ground) are shown with a red line and weather GPV data (10 m above ground) are shown with a blue line, both in the same graph. Regarding the wind direction corresponding to the above, because there are no measured data, only weather GPV data are shown. Regarding the comparison between the wind speeds of the measured data and those of weather GPV data, no large variations are observed in the reproduction of weather GPV data; however, the variations in association with daily wind speed variation are well reproduced. Figure 3 shows the daily variations of wind speed and wind direction during the period from December 2014 to January 2015 as a sample of the data in the winter. As

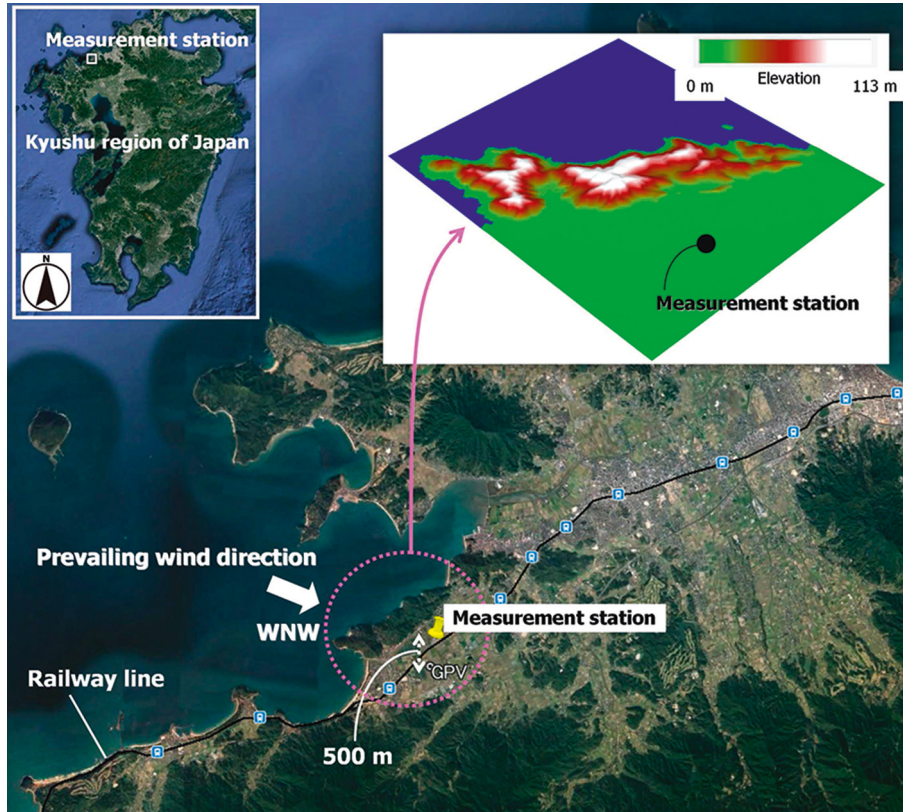


FIGURE 1: Locations of the railway line and observation mast and evaluation points of weather GPV data existing around the observation station.

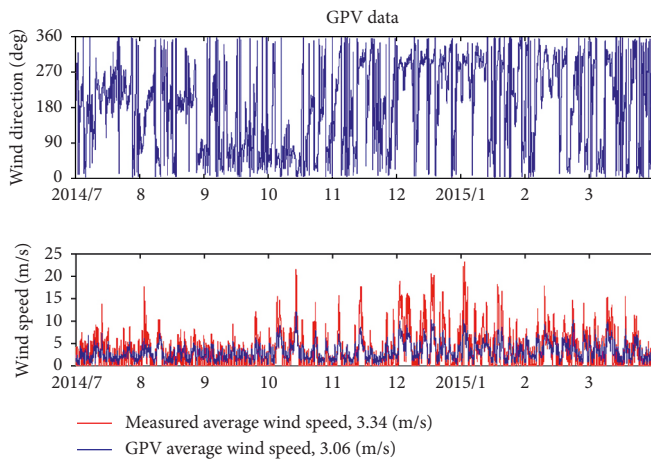


FIGURE 2: Comparison of measured data (5 m above ground) and weather grid point value (GPV) data (10 m above ground) for nine months from July 2014 to March 2015.

described in Figure 2, the comparison of wind speed shows that no large variations are observed in the reproduction of weather GPV data (10 m above ground) as observed in measured data (5 m above ground); however, the variations in association with daily wind speed are well reproduced. As will be explained later in detail, it can be understood that the appearance frequency of wind direction (shown with a red frame) in the north-northwest (defined angles clockwise

between 281.25 degrees or more and less than 303.75 degrees) is high. Figure 4 shows a scatter plot relating to the wind speed data of the measured data and weather GPV data. The correlation coefficient is approximately 0.9 (see formula (1)), which shows that there is a strong correlation between the measured data (5 m above ground) and weather GPV data (10 m above ground). As there is a strong correlation between the wind speeds of both data, the wind data of the weather GPV were used as the wind direction data corresponding to the measured data in this research. A wind rose (nine months for whole period for data collected from July 2014 to March 2015) is shown in Figure 5, in which the time-series data set consisting of the measured data (5 m above ground) and corresponding wind direction of weather GPV data (10 m above ground) was evaluated. As described in Figure 3, closer scrutiny of this figure showed that the appearance frequency of the wind from the west-northwest was extremely high, and it was defined as the main wind direction of this area. Based on the result of the analysis of Figure 5, all data falling under the wind direction range of the west-northwest were consecutively arranged in the time direction, as shown in Figure 6. There were 773 data points falling under the wind direction range of west-northwest, and they accounted for approximately 12% of all data. The average wind speed of the 773 data points was approximately 8.7 m/s, and the corresponding turbulence intensity was 57%; it was clarified that both showed high values. From the above result, it was quantitatively shown that when the

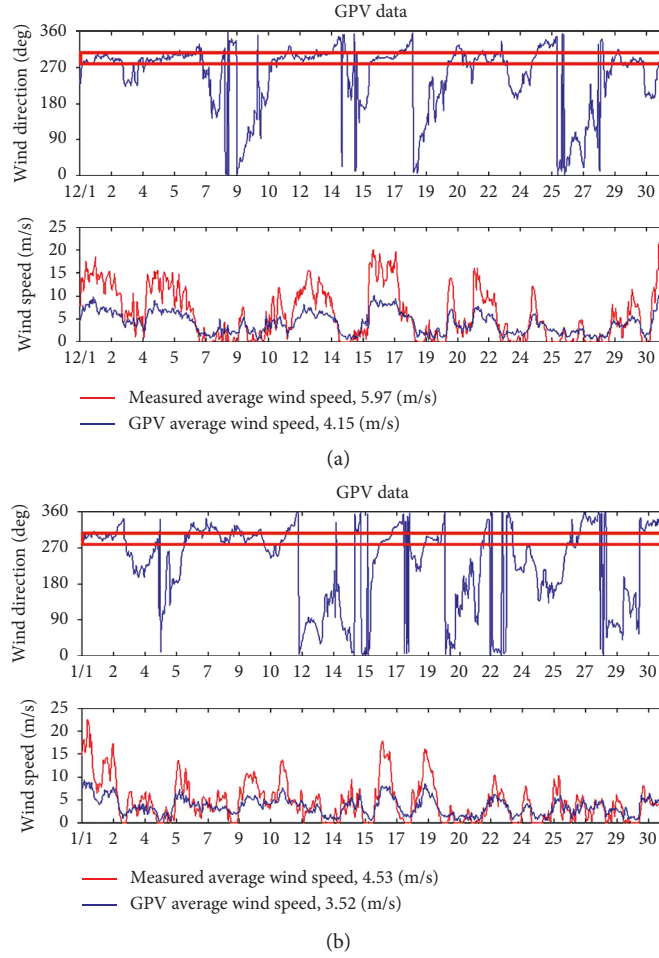


FIGURE 3: Comparison of measured data (5 m above ground) and weather GPV data (10 m above ground). (a) December 2014. (b) January 2015.

winds from west-northwest blew in this area, a local strong wind area was generated. In the next section, a computational simulation of wind conditions targeting the wind from west-northwest by LES will be conducted, and the generation mechanism of the local strong wind area will be discussed in detail.

$$r_{xy} = \frac{1/n \sum_{i=1}^n (x_i - \bar{x})(y_i - \bar{y})}{\sqrt{1/n \sum_{i=1}^n (x_i - \bar{x})^2} \sqrt{1/n \sum_{i=1}^n (y_i - \bar{y})^2}} \quad (1)$$

Average wind speeds by wind direction (solid line) from measured data and wind direction appearance frequency (dotted line) from weather GPV data.

3. Outline of Numerical Calculation Technique

In this research, in order to avoid numerical instability and predict the local flow of wind in a complex terrain with high accuracy, a collocated grid of the generalized curvilinear coordinate system was used. Regarding the numerical calculation technique, based upon a finite-difference method (FDM), a large-eddy simulation (LES) was employed as the turbulence model. In the case of LES, a spatial filter is

provided in the flow field, and grid scale (GS) eddies larger than the computational cell and subgrid scale (SGS) eddies smaller than GS eddies and are separated from the turbulent flow eddies of various sizes. GS large eddies are numerically simulated directly, independent of the physical model. Meanwhile, the energy dissipation action carried out by SGS small eddies was modeled mainly on the physical consideration of SGS stress. Please refer to the past literature for the detailed calculation method.

The calculating area in this research has a space of 12.3 (x) × 3.5 (y) × 0.65 (z) km, in the main stream direction (x), in the right-angled direction to the main stream (y), and in the vertical direction (z). The maximum altitude in the calculating area was 180 m, and the minimum latitude was 0 m. A 3D shape of the complex terrain was reproduced based on the data with a spatial resolution of 10 m from the Geospatial Information Authority of Japan (GSI). The number of computational cells was approximately 18 million, with a total number of 1,231 (x) × 351 (y) × 41 (z) in each direction. The grid widths in the x direction and y direction were assumed to be 10 m at uniform intervals. The grid width was nonuniform in the z direction so that the density of grid points increased smoothly toward the ground

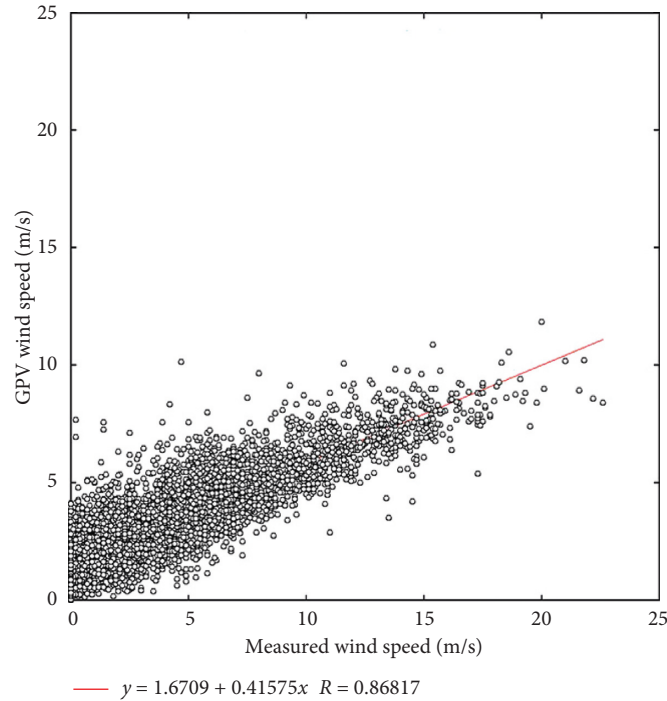


FIGURE 4: Scatter plot of measured data (5 m above ground) and weather GPV data (10 m above ground) for nine months from July 2014 to March 2015.

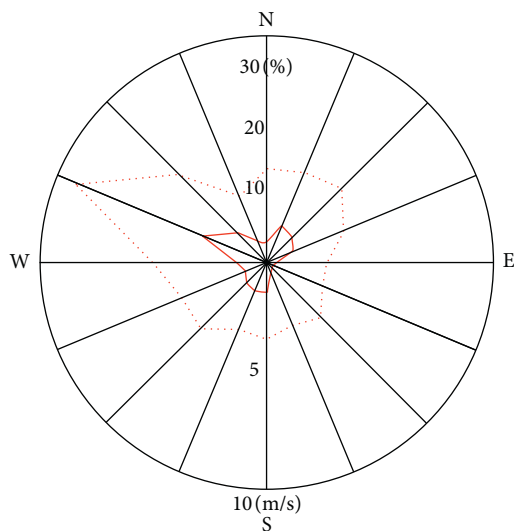


FIGURE 5: Wind rose for nine months from July 2014 to March 2015.

surface ($\Delta z_{\min} = 0.5 \text{ m}$). As mentioned above, the targeted wind direction in the area for research was presumed to be west-northwest. This wind direction is the main wind direction in this area. Regarding boundary conditions, a wind speed distribution following the power law (N value = 20) was applied to the inlet boundary surface. A sliding condition was applied to the side boundary surface and upper boundary surface, and a convective outflow condition was applied to the outflow boundary surface. A no-slip condition was applied to the ground surface. The Reynolds number, a

dimensionless parameter, was assumed to be $Re = 10^4$ in this simulation, and the dimensionless time step was assumed to be 0.002.

4. Calculation Results and Discussion

Figure 7 shows the wind speed distribution in the direction of the main stream (x) (instantaneous flow field, horizontal cross-section 5 m above ground), as the result of a computational simulation of wind conditions, projected onto Google Earth. It can be observed that the neighborhood of the observation mast is strongly affected by the separated flow (complex turbulent field) originating from the small-scale terrain positioned at the side of the upstream (at an altitude of approximately 180 m).

Figure 8 shows a wind speed distribution (instantaneous flow field, vertical cross-section passing observation mast) in the main stream direction. From this figure, it can also be seen that the neighborhood of the observation mast is directly affected by a separate flow originating from the small-scale terrain (at an altitude of approximately 180 m) positioned upstream nearby. In particular, a separated flow originating from the small-scale terrain adheres to the ground; along with that, a very strong wind area is formed locally, and it can be observed that it passes through the observation mast (the area boxed with black lines in the figure).

Figure 9 shows the time variation of the wind direction (angle) within the horizontal cross-section of the wind passing through the observation mast (5 m above ground). In this figure, two red lines are drawn, showing

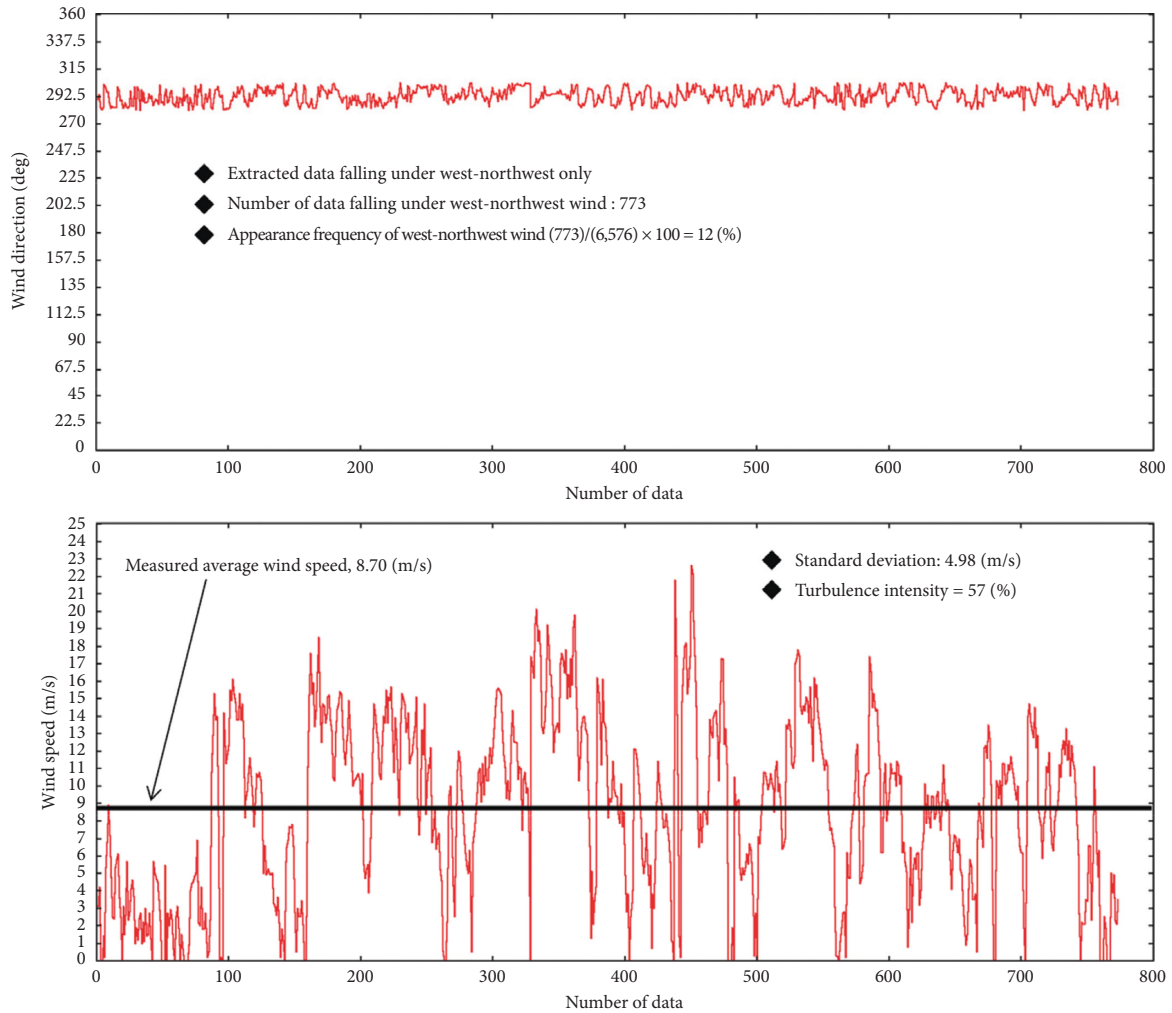


FIGURE 6: West-northwest wind speed data (defined angles clockwise between 281.25 degrees or more and less than 303.75 degrees), consecutively arranged in time direction.



FIGURE 7: Wind speed distribution in the mainstream direction x , instantaneous flow field, and horizontal cross-section 5 m above ground.

± 25 degrees. By scrutinizing this figure, it can be observed that changes in wind direction over 25 degrees in the horizontal direction often occur, which suggests that

this exerts a large wind load on trains. The prediction of the occurrence of nonsteady wind load and possible countermeasures will become even more important in the future from the viewpoint of safe operation of trains.

Figure 10 shows the time variation of the wind speed by a computational simulation of wind conditions (5 m above ground). The values were converted so that the average value of the wind speed equals that obtained from the measured values (approximately 8.7 m/s) shown in Figure 6. Focusing on the time history waveform of wind speed, it was shown that large airflow changes occur simultaneously in the measured data of Figure 6. As a result, the turbulent intensity calculated from the computational simulation of wind conditions also showed very large values (approximately 32%), similar to the measured data. From the above results, it was suggested that the very large turbulence intensity (approximately 57%) obtained from the measured data of Figure 6 was mainly caused by the separated flow originating from the small-scale terrain (at latitude of approximately 180 m) positioned at the upstream site.

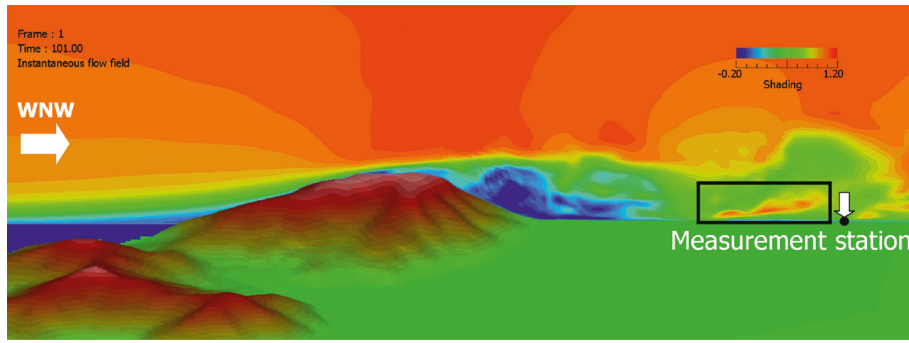


FIGURE 8: Wind speed distribution in the mainstream direction x , instantaneous flow field, and vertical cross section passing through the observation mast.

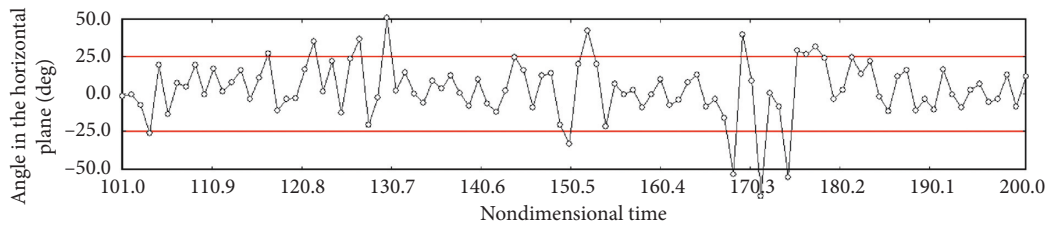


FIGURE 9: Time variation of wind direction (angle) within the horizontal cross section of the wind passing through the observation mast at 5 m above ground.

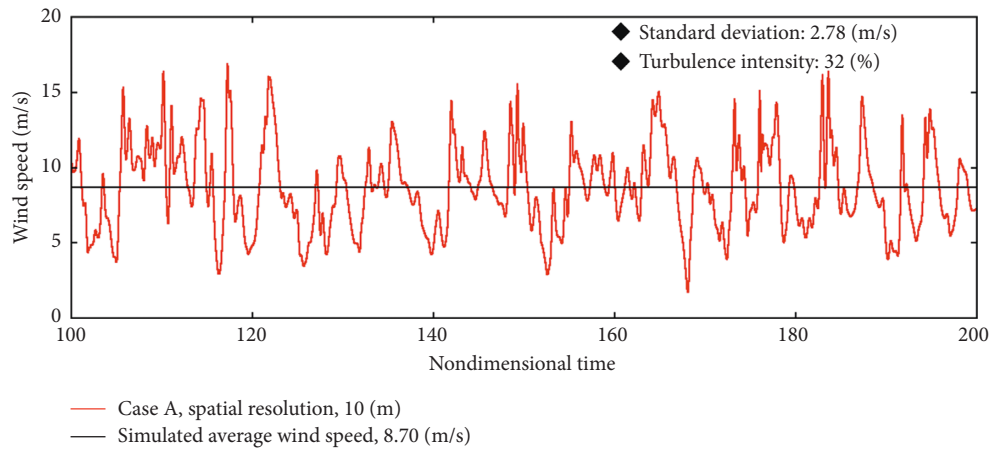


FIGURE 10: Time variation of wind speed by a computational simulation of wind conditions, with a spatial resolution of 10 m at 5 m above ground.

5. Effects of Size of Calculation Area and Grid Resolution in the Horizontal Direction

Computational simulations of wind conditions were implemented by changing the size of the calculation area and grid resolution in the horizontal direction, and the effects of these calculation parameters on the accuracy of the reproduction of the area of local wind conditions were discussed. As shown in Figure 11, a space of 3.0 (x) \times 2.5 (y) \times 0.65 (z) km in the main stream direction (x), in the right-angled direction to the main stream (y), and the vertical direction (z) was set up for the calculation area. The size of the area in the z direction is the same as that of Figure 12, and the maximum altitude (180 m) and the minimum altitude

(0 m) in the calculation area also are the same as those of Figure 12. The terrain altitude data were also based upon those of a spatial resolution of 10 m of the Geospatial Information Authority of Japan (GSI). Regarding the computational cells, the grid widths in the x direction and y direction were assumed to be as large as two times the spatial resolution of Figure 12, at uniform intervals of 5 m. The grid width was nonuniform in the z direction so that the density of grid points increased smoothly toward the ground surface. The minimum grid width in the vertical direction was 0.5 m, similar to that of Figure 12. The total number of computational cells was approximately 12 million, with 601 (x) \times 501 (y) \times 41 (z) in each direction. Associated with the increase of the grid resolution in the horizontal direction, the

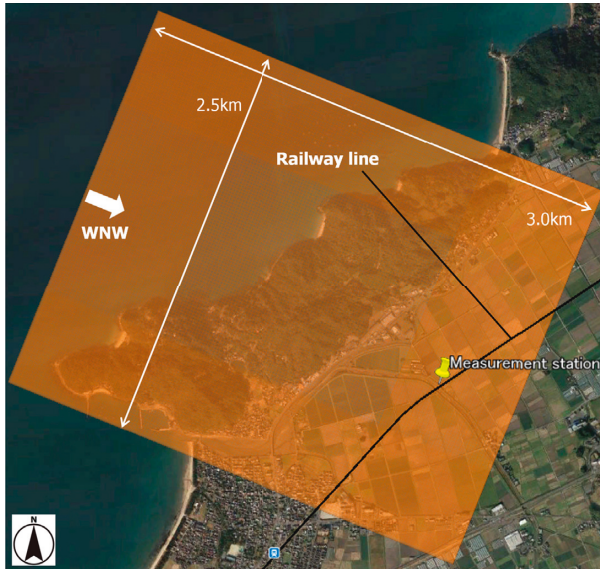


FIGURE 11: Calculation area when grid resolution in the horizontal direction was increased.



FIGURE 12: Calculation area and others.

dimensionless time step was set to 0.0001. Other initial conditions and boundary conditions were the same as those of the computational simulation of wind conditions, as mentioned previously.

Figure 13 shows the comparison of time variations of wind speed at resolutions of 10 m and 5 m (at 5 m above ground). The values were converted so that the average values of wind speed (dimensionless quantity) were equal to those obtained from the measured values (approximately 8.7 m/s) shown in Figure 6. Focusing on the time history of the waveform, no significant difference was observed between the calculation results at spatial resolutions of 10 m and 5 m. Regarding turbulent intensity, approximately the same result was obtained. From the above, it was clarified that, when the air flow characteristics of the separated flow originating from the small-scale terrain targeted in this research (at an altitude of approximately 180 m) is reproduced with high accuracy, the spatial resolution of the computational cells in the horizontal direction needs to be approximately 10 m.

6. Effect of Atmospheric Stability

Generally, the atmospheric boundary layer has a stratified state, where the concentration of density (or temperature) changes in the vertical direction, and the flow in the ground inversion layer, which often occurs at night, forms a stably stratified flow, where the density decreases at higher altitudes (as the temperature becomes high). It is known that when the stably stratified flows pass through ground structures, simple terrain, or complex terrain, a negative buoyancy acts on the flow field and various wave phenomena and flow phenomena occur. The wave phenomena and flow phenomena that occur at stably stratified fields are related to topographic strong wind disasters (local strong wind disasters), and they are as important issues as environmental problems at the time of strong wind. In the region targeted in this research, air currents passing above the sea during winter invaded into the small-scale terrain (at an altitude of approximately 180 m), so that the safely stratified state should be considered. Therefore, in this research, the authors focused on atmospheric stability, where lee waves (internal gravity waves) were excited at the downstream side of the small-scale terrain (at an altitude of approximately 180 m) and discussed the speed increasing rate of the local strong wind areas which were induced. The speed increase rate is the average value of wind speed at the time of stable stratification at 5 m above ground divided by the average value of wind speed at a neutral time; the averaging time is dimensionless time 10. The dimensionless parameter relating to atmospheric stability used in this research is the Froude number ($=U/Nh$). Here, U is wind speed, h is the height of the terrain, and N is buoyancy frequency.

Figure 14 shows the result of the visualization of the stably stratified flows ($Fr \approx 1.0$ and 0.5) moving beyond isolated peaks visualized by using the towing water tank. In Figure 14(a), lee waves of long wavelengths are formed in the downstream of the terrain, and at the same time, ground-based rotors are formed close to the ground. In Figure 14(b), where the flows were more stably stratified, the wave lengths of the lee wave become short, and at the same time, it can be observed that an elevated rotor is formed above the downstream of the terrain corresponding to the ground-based rotors.

Figure 15 shows the result of the computational simulation of wind conditions (instantaneous flow field, $Fr = 1.0$ and 0.5) conducted under similar conditions to Figure 14, as shown above. Figure 15 shows a streamline view drawn as the trajectories of visual particles released from the upper stream of the terrain and the distribution of wind speeds in the mainstream direction (x). A review of Figure 15 shows that the wave patterns, ground-based rotors, and elevated rotor obtained by the water-tank experiment are reproduced there, and it was confirmed that the computational simulation program of wind conditions reproduced the stably stratified flows passing through the terrain very well. From the above, it was determined to apply this program to actual complex terrains.

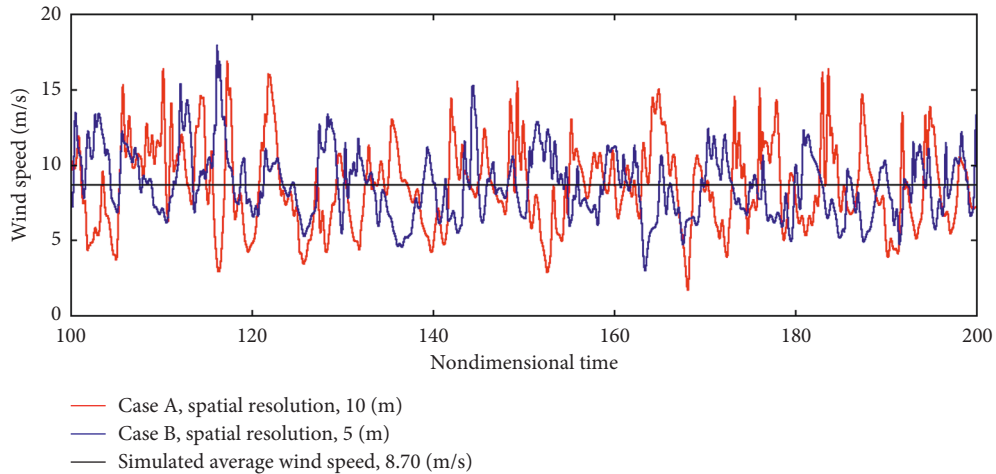


FIGURE 13: Time variation of wind speed in the computational simulation of wind conditions and comparison of spatial resolutions of 10 m and 5 m at 5 m above ground.

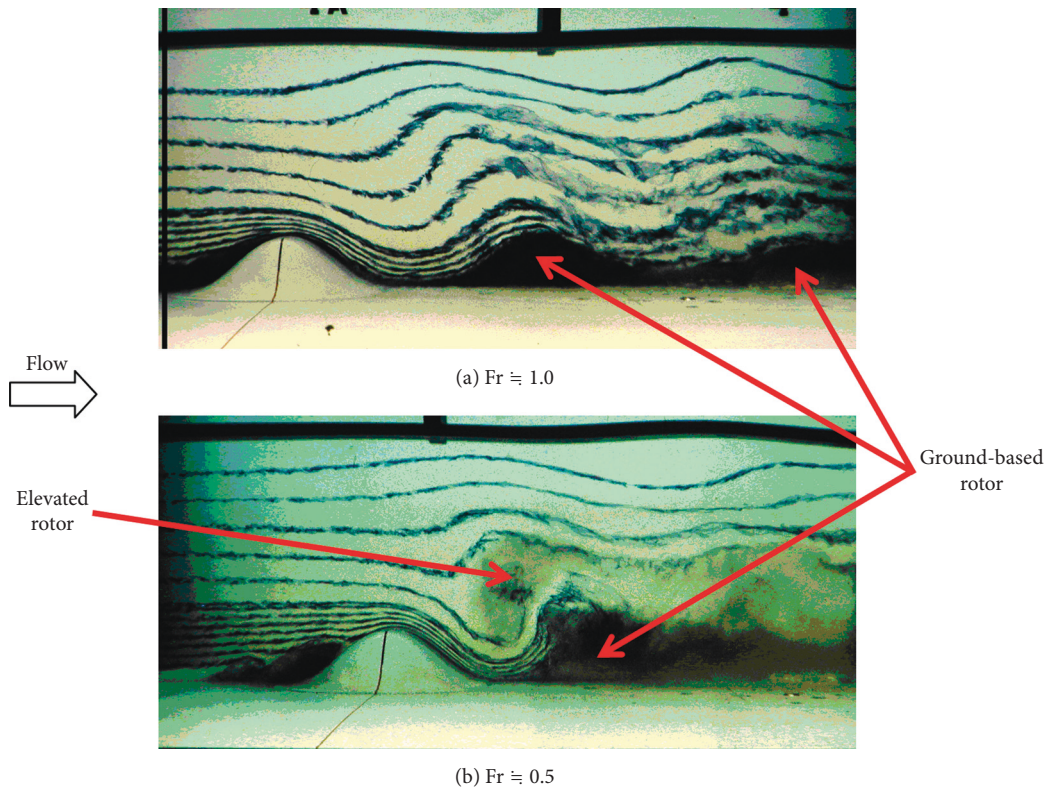


FIGURE 14: Result of visualization using a towing water tank (Hunt and Snyder [29]).

Figure 16 shows the result of the computational simulation of wind conditions of stably stratified flows (wind direction is WNW, $Fr = 1.0$) conducted, targeting the calculation area shown in Figure 11 (grid resolution 5 m in horizontal direction). Figure 16 shows the time variation in the wind condition area at a dimensionless time interval of 2.5. Lee waves are excited at the downstream of the terrain over time. Additionally, the reverse-flow region lying behind the terrain that had been observed at the neutral time in Figure 8 is inhibited. As a result, in the downstream of the

terrain, a local strong wind area occurs, as shown by an arrow, and the strong wind area passing through the observation mast can be observed. The increasing rate of speed in the local strong wind area induced under stable stratification was discussed, and it was clarified that wind approximately 1.2 times as strong as that at neutral time was generated. The speed increasing rate is the average wind speed value under stable stratification at 5 m above ground divided by the average value of wind speeds at a neutral time; the averaging time is dimensionless time 10.

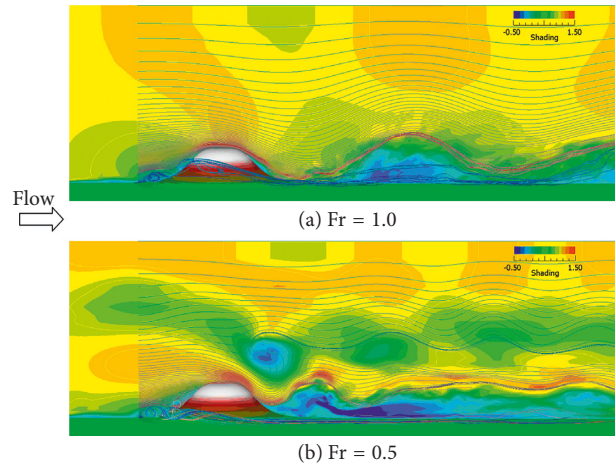


FIGURE 15: Result of visualization by computational simulation of wind conditions, $Re = 10^4$.

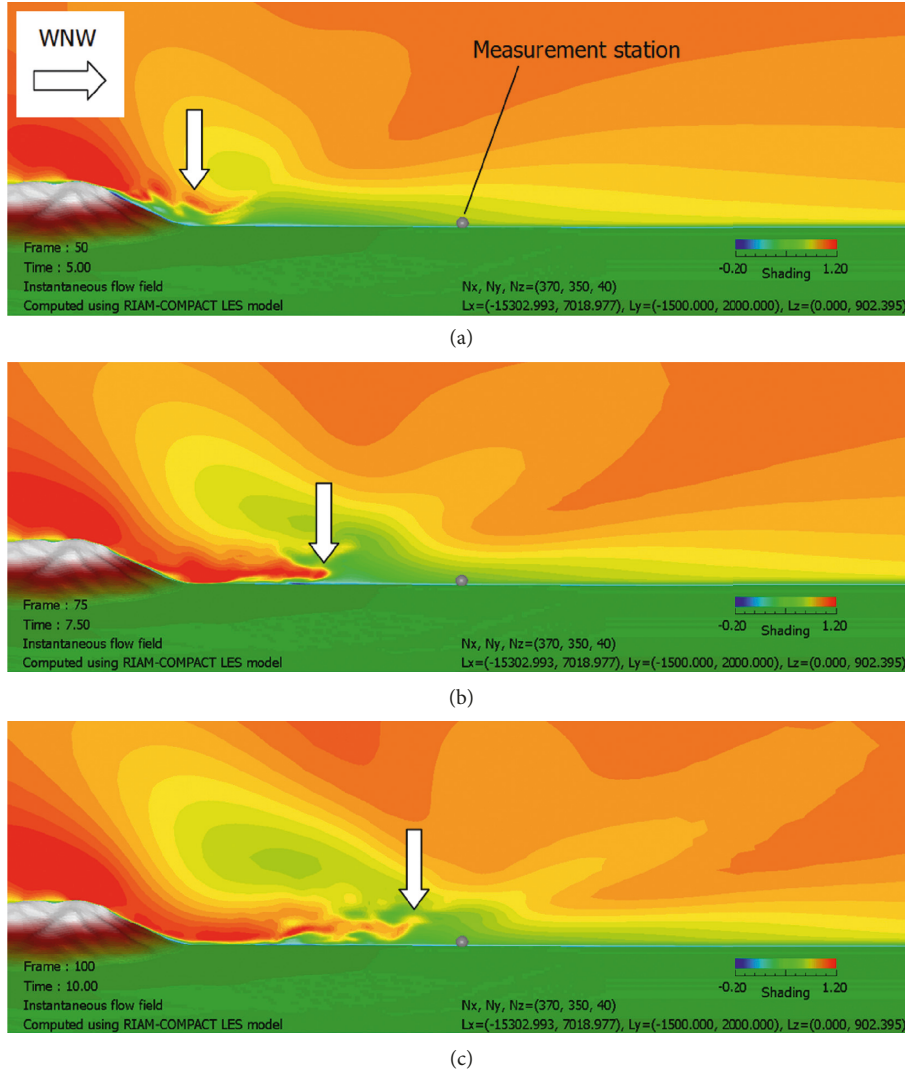
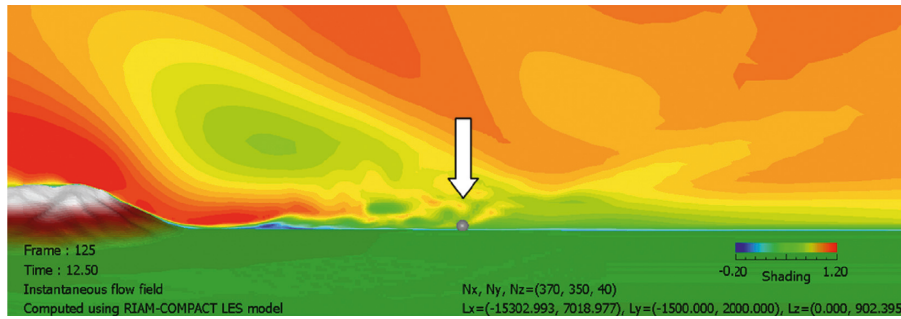


FIGURE 16: Continued.



(d)

FIGURE 16: Result of the computational simulation of wind conditions of stably stratified flow targeting the actual complex terrain.

7. Conclusions

In this research, a computational fluid dynamics (CFD) approach, which has been used in wind power generation fields, was applied as a solution for the problems of local strong wind areas in railway fields. The mechanism of wind generation was discussed, and at the same time, the effectiveness of its application to railway fields was discussed. The problem of the strong local wind that occurs on the railway line in winter was taken up in this research. In the railway line, train delays at the time of strong winds in the winter often cause problems. Against this problem, the characteristics of the wind conditions of the local strong wind area generated around the railway line were discussed based on the measured data and the weather GPV data. As a result of the investigation, it was shown that the direction of this strong wind was west-northwest. Then, a computational simulation of wind conditions targeting this wind from the west-northwest by LES was implemented, and it was clarified that the local strong wind area was mainly caused by the separated flow originating from the small-scale terrain (at an altitude of approximately 180 m) positioned at its upstream side. At the time, the effects of the size of the calculation area and spatial grid resolution on the result of the calculation and the effect of atmospheric stability were also discussed. It was clarified that, when the air flow characteristic of the separated flow originating from the small-scale terrain (at altitude of approximately 180 m) targeted in this research is to be reproduced with high accuracy by the computational simulation of wind condition characteristics, approximately 10 m of spatial resolution of the computational cell in the horizontal direction is required. As a result of the computational simulation of wind conditions of the stably stratified flow ($Fr = 1.0$), lee waves were excited at the downstream of the terrain over time. As a result, the reverse-flow region lying behind the terrain that had been observed at the neutral time was inhibited. This generated a local strong wind area at the downstream of the terrain, and the strong wind area passing through the observation mast was observed. The investigation of the increasing rate of speed of the local strong wind area induced at the time of stable stratification showed that a wind approximately 1.2 times as strong as that at a neutral time was generated. The speed increasing rate is the average wind speed value under stable stratification at

5 m above ground divided by the average value of wind speed at a neutral time; the averaging time is dimensionless time 10.

Data Availability

The data used to support the findings of this study are available from the corresponding author upon request.

Conflicts of Interest

The authors declare that they have no conflicts of interest.

Acknowledgments

This research was supported by a joint research with Kyushu Railway Company, a research project assigned by West Japan Railway Company, and a joint research project with Railway Technical Research Institute. The authors strongly appreciate the cooperation.

References

- [1] R. Rodrigues and C. Lengsfeld, "Development of a computational system to improve wind farm layout, Part I: model validation and near wake analysis," *Energies*, vol. 12, no. 5, p. 940, 2019.
- [2] A. Gargallo-Peiró, M. Avila, H. Owen, L. Prieto-Godino, and A. Folch, "Mesh generation, sizing and convergence for onshore and offshore wind farm atmospheric boundary layer flow simulation with actuator discs," *Journal of Computational Physics*, vol. 375, pp. 209–227, 2018.
- [3] M. Sessarego, W. Shen, M. Van der Laan, K. Hansen, and W. Zhu, "CFD simulations of flows in a wind farm in complex terrain and comparisons to measurements," *Applied Sciences*, vol. 8, no. 5, p. 788, 2018.
- [4] O. Temel, L. Briceux, and J. van Beeck, "Coupled WRF-OpenFOAM study of wind flow over complex terrain," *Journal of Wind Engineering and Industrial Aerodynamics*, vol. 174, pp. 152–169, 2018.
- [5] F. Castellani, M. Buzzoni, D. Astolfi, G. D'Elia, G. Dalpiaz, and L. Terzi, "Wind turbine loads induced by terrain and wakes: an experimental study through vibration analysis and computational fluid dynamics," *Energies*, vol. 10, no. 11, p. 1839, 2017.

- [6] K. S. R. Murthy and O. P. Rahi, "A comprehensive review of wind resource assessment," *Renewable and Sustainable Energy Reviews*, vol. 72, pp. 1320–1342, 2017.
- [7] T. Simões and A. Estanqueiro, "A new methodology for urban wind resource assessment," *Renewable Energy*, vol. 89, pp. 598–605, 2016.
- [8] H. Gopalan, C. Gundling, K. Brown et al., "A coupled mesoscale-microscale framework for wind resource estimation and farm aerodynamics," *Journal of Wind Engineering and Industrial Aerodynamics*, vol. 132, pp. 13–26, 2014.
- [9] T. F. Ishugah, Y. Li, R. Z. Wang, and J. K. Kiplagat, "Advances in wind energy resource exploitation in urban environment: a review," *Renewable and Sustainable Energy Reviews*, vol. 37, pp. 613–626, 2014.
- [10] F. Porté-Agel, Y.-T. Wu, and C.-H. Chen, "A numerical study of the effects of wind direction on turbine wakes and power losses in a large wind farm," *Energies*, vol. 6, no. 10, pp. 5297–5313, 2013.
- [11] J. M. L. M. Palma, F. A. Castro, L. F. Ribeiro, A. H. Rodrigues, and A. P. Pinto, "Linear and nonlinear models in wind resource assessment and wind turbine micro-siting in complex terrain," *Journal of Wind Engineering and Industrial Aerodynamics*, vol. 96, no. 12, pp. 2308–2326, 2008.
- [12] T. Uchida, "Numerical investigation of terrain-induced turbulence in complex terrain using high-resolution elevation data and surface roughness data constructed with a drone," *Energies*, vol. 12, no. 19, p. 3766, 2019.
- [13] T. Uchida and Y. Kawashima, "New assessment scales for evaluating the degree of risk of wind turbine blade damage caused by terrain-induced turbulence," *Energies*, vol. 12, no. 13, p. 2624, 2019.
- [14] T. Uchida and S. Takakuwa, "A large-eddy simulation-based assessment of the risk of wind turbine failures due to terrain-induced turbulence over a wind farm in complex terrain," *Energies*, vol. 12, no. 10, p. 1925, 2019.
- [15] T. Uchida, "Numerical investigation of terrain-induced turbulence in complex terrain by large-eddy simulation (LES) technique," *Energies*, vol. 11, no. 10, p. 2638, 2018.
- [16] T. Uchida, "Computational fluid dynamics approach to predict the actual wind speed over complex terrain," *Energies*, vol. 11, no. 7, p. 1694, 2018.
- [17] T. Uchida, "LES investigation of terrain-induced turbulence in complex terrain and economic effects of wind turbine control," *Energies*, vol. 11, no. 6, p. 1530, 2018.
- [18] T. Uchida, "Computational fluid dynamics (CFD) investigation of wind turbine nacelle separation accident over complex terrain in Japan," *Energies*, vol. 11, no. 6, p. 1485, 2018.
- [19] T. Uchida and Y. Ohya, "Micro-siting technique for wind turbine generators by using large-eddy simulation," *Journal of Wind Engineering and Industrial Aerodynamics*, vol. 96, no. 10-11, pp. 2121–2138, 2008.
- [20] T. Uchida and Y. Ohya, "Large-eddy simulation of turbulent airflow over complex terrain," *Journal of Wind Engineering and Industrial Aerodynamics*, vol. 91, no. 1-2, pp. 219–229, 2003.
- [21] T. Uchida and Y. Ohya, "Numerical simulation of atmospheric flow over complex terrain," *Journal of Wind Engineering and Industrial Aerodynamics*, vol. 81, no. 1–3, pp. 283–293, 1999.
- [22] Y. Misu and T. Ishihara, "Prediction of frequency distribution of strong crosswind in a control section for train operations by using onsite measurement and numerical simulation," *Journal of Wind Engineering and Industrial Aerodynamics*, vol. 174, pp. 69–79, 2018.
- [23] O. Pons, A. de la Fuente, J. Armengou, and A. Aguado, "Towards the sustainability in the design of wind towers," *Energy Procedia*, vol. 115, pp. 41–49, 2017.
- [24] T. Fukuhara, S. Tanimoto, and K. Araki, "Methods to estimate spatial distribution of local meteorological conditions along railway line," *Quarterly Report of RTRI*, vol. 57, no. 4, pp. 268–274, 2016.
- [25] K. Araki, T. Fukuhara, T. Shimamura, and T. Imai, "Method for detecting railway line sections exposed to strong winds using numerical simulations," *Quarterly Report of RTRI*, vol. 52, no. 1, pp. 27–33, 2011.
- [26] M. Burlando, A. Freda, C. F. Ratto, and G. Solari, "A pilot study of the wind speed along the Rome-Naples HS/HC railway line. Part 1-numerical modelling and wind simulations," *Journal of Wind Engineering and Industrial Aerodynamics*, vol. 98, no. 8-9, pp. 392–403, 2010.
- [27] A. Freda and G. Solari, "A pilot study of the wind speed along the Rome-Naples HS/HC railway line: Part 2—probabilistic analyses and methodology assessment," *Journal of Wind Engineering and Industrial Aerodynamics*, vol. 98, no. 8-9, pp. 404–416, 2010.
- [28] T. Takemi, K. Kusunoki, K. Araki et al., "Representation and localization of gusty winds induced by mesocyclones with a high-resolution meteorological modeling," *Theoretical and Applied Mechanics Japan*, vol. 58, pp. 121–130, 2010.
- [29] J. C. R. Hunt and W. H. Snyder, "Experiments on stably and neutrally stratified flow over a model three-dimensional hill," *Journal of Fluid Mechanics*, vol. 96, no. 4, pp. 671–704, 1980.

